Effect of Uncertainty in Blowing Ratio on Film Cooling Effectiveness

Hessam Babaee
Department of Mechanical Engineering,
Louisiana State University,
Baton Rouge, LA 70803
e-mail: hbabae1@lsu.edu

Xiaoliang Wan
Assistant Professor
Department of Mathematics,
Louisiana State University,
Baton Rouge, LA 70803
e-mail: xlwan@math.lsu.edu

Sumanta Acharya
Professor
Department of Mechanical Engineering,
Louisiana State University,
Baton Rouge, LA 70803
e-mail: acharya@tigers.lsu.edu

In this study, the effect of randomness of blowing ratio on film cooling performance is investigated by combining direct numerical simulations with a stochastic collocation approach. The geometry includes a 35-deg inclined jet with a plenum attached to it. The blowing ratio variations are assumed to have a truncated Gaussian distribution with mean of 0.3 and the standard variation of approximately 0.1. The parametric space is discretized using multi-element general polynomial chaos (ME-gPC) with five elements where general polynomial chaos of order 3 is used in each element. Direct numerical simulations were carried out using spectral element method to sample the governing equations in space and time. The probability density function of the film cooling effectiveness was obtained and the standard deviation of the adiabatic film cooling effectiveness on the blade surface was calculated. A maximum of 20% of variation in film cooling effectiveness was observed at 2.2 jet-diameter distance downstream of the exit hole. The spatially-averaged adiabatic film cooling effectiveness was 0.23 ± 0.02. The calculation of all the statistical properties were carried out as off-line post processing. A fast convergence of the polynomial expansion in the random space is observed which shows that the computational strategy is very cost-effective. [DOI: 10.1115/1.4025562]

Keywords: film cooling, uncertainty quantification, polynomial chaos

1 Introduction

Increasing the turbine inlet temperature directly increases the thermal efficiency of a gas turbine. However, the temperature of the inlet gas is limited by the melting point of the blade metal. To allow higher inlet gas temperatures, film cooling has been widely used in modern gas turbines [1]. In film cooling technology, the coolant flow is extracted after the compressor and is injected through holes on the surface of the hot-gas components. However as a result of variability in operating conditions, the performance of film cooling can be unfavorably affected leading to the exposure of the hot-gas components to high temperatures beyond the permissible limit. This has severe impact on the gas turbine durability where increasing the airfoil temperature by 25 °C can reduce the life time of a blade by a factor of two [2]. The cost of the replacement of vane/blade airfoils is high, most of which is attributed to the manufacture or repair of the film cooling holes.

Film cooling effectiveness, among other factors, is strongly dependent on the blowing ratio (the ratio of the averaged coolant velocity in the delivery tube to the crossflow velocity) as demonstrated by several experimental and numerical studies (see for e.g., Refs. [3,4]). The coolant film with very low blowing ratio ($BR < 0.1$) can be rapidly mixed out with the crossflow, which leads to the deterioration of film cooling performance. Higher blowing ratios ($BR > 1$), on the other hand, cause the jet to lift off from the surface, which allows the hot gas from the crossflow to penetrate into the separated region downstream of the jet, resulting in a poor coverage of the blade surface. Intuitively, a blowing ratio exists which results in the best film cooling effectiveness, and the existence of an optimal blowing ratio that maximizes film cooling for specific operating conditions and geometry (typically a flat plate) has been reported in the literature. The optimum blowing ratio can vary depending on the operating conditions and geometry, and designers use empirical data and experience in designing the set-points for the film cooling parameters.

In practice, the blowing ratio is far from its designed value. Abhari [5] reported the coolant fluctuations of up to $\pm 100\%$ around the design blowing ratio due to rotor-stator interactions. Experimental measurements carried out by Womack et al. [6] showed that the blade heat transfer coefficient was significantly affected by the presence of wakes in the crossflow; this variation is, in part, due to variations in the blowing ratio. Thus, it is important to investigate the effect of blowing ratio variation on the cooling effectiveness.

As a numerical strategy in stochastic computations, Monte Carlo methods and its variants are of the most widely used approaches. This family of methods requires sampling of the deterministic system at random inputs. Monte Carlo methods are especially attractive when a large number of random variables are considered, since their convergence rates do not depend or weakly depend on the number of random dimensions. However, Monte Carlo methods are prohibitively expensive for our problem, where each sample requires solving an expensive direct numerical simulation (DNS) with several millions degree of freedom.

In cases with only a few random variables, spectral methods in which the target function is represented as an expansion of fast-converging polynomials, can be far more efficient, especially when the functional relationship between the random variable and the target function is smooth. The spectral methods are relatively new in the field of stochastic computation and they have enjoyed a rapid growth in the last decade in the numerical simulation of random/stochastic partial differential equations [7]. The first variant of these approaches is the polynomial chaos (PC) where the Hermite polynomials constitute an orthogonal expansion basis of the probability space. The coefficients of the expansion are obtained by employing a Galerkin projection. This method was pioneered by Ghanem and Spanos [8] for solving stochastic differential equations and was extended by Xiu and Karniadakis [9] to gPC which includes a broader family of polynomials from the Asky scheme. The gPC method was successfully used to solve Navier-Stokes equations with random inflows [10]. In cases where

Contributed by the Heat Transfer Division of ASME for publication in the Journal of Heat Transfer. Manuscript received April 27, 2013; final manuscript received August 18, 2013; published online November 15, 2013. Assoc. Editor: Phillip M. Ligrani.

sufficient smoothness between the input random variable and the target random function does not exist, increasing polynomial order can be inefficient [11]. To remedy this limitation, Wan and Karniadakis [12] developed a multi-element extension (ME-gPC) to the general polynomial chaos, in which the random space is first decomposed into a number of finite elements. Within each element an orthogonal polynomial expansion is employed; this is a concept analogous to the spectral element approach that has been used for deterministic problems.

One of the main considerations in studying the effect of uncertainty in film cooling applications is the computational cost of solving such a problem. The dynamics of film cooling problem is properly studied as a jet-in-crossflow, where the interaction of the coolant jet and the hot gas creates a highly unsteady and in most cases turbulent flow. This problem has been extensively studied both numerically and experimentally. The majority of the numerical simulations have utilized Reynolds averaged Navier-Stokes equations which rely on turbulence models. These models have been shown to be unsuitable to accurately capture the dynamics of the flow and high-fidelity numerical simulations that resolve the relevant spatial and temporal scales in the flow are required [13]. Large eddy simulation (LES) has been shown to be a reliable tool in solving film cooling problems [14–18] by resolving the large scale structures and modeling the smaller scales. Nevertheless using any turbulence model brings a new source of uncertainty to the problem that unless it is quantified, can interfere with the randomness imposed by the boundary condition such as blowing ratio. DNS, on the other hand, resolves all relevant time and space scales without using a model and it has been successfully used to simulate turbulent flows in film cooling [19,20].

The goal of the current study is to investigate the effect of the uncertainty in the blowing ratio on the film cooling effectiveness. We present a computationally affordable strategy to investigate the effect of randomness in blowing ratio on the performance of film cooling. We combine DNS using spectral/hp finite element method and ME-gPC method as a strategy to discretize the parametric space. The film-cooling geometry includes a flat surface with a 35-deg inclined coolant delivery tube fed by a plenum. The outcome of this study will enable us to quantify the effect of randomness in blowing ratio on the surface temperature or cooling effectiveness. To the best knowledge of the authors, this is the first study that investigates film cooling in a probabilistic framework. Moreover, the discretization strategy provides some inherent advantages in computational efficiency that is discussed in the paper.

2 Problem Specification

We solve the incompressible Navier-Stokes equations for velocity and pressure along with the advection-diffusion equation for temperature. These equations in nondimensional form are given by

$$\nabla \cdot \mathbf{u} = 0 \tag{1}$$

$$\frac{\partial \mathbf{u}}{\partial t} + (\mathbf{u} \cdot \nabla)\mathbf{u} = -\nabla p + \frac{1}{\mathrm{Re}}\nabla^2 \mathbf{u} \tag{2}$$

$$\frac{\partial \theta}{\partial t} + (\mathbf{u} \cdot \nabla)\theta = \frac{1}{\mathrm{RePr}}\nabla^2 \theta \tag{3}$$

where $\mathbf{u} = \mathbf{u}(\mathbf{x}, t; \xi)$, $p = p(\mathbf{x}, t; \xi)$, and $\theta = \theta(\mathbf{x}, t; \xi)$ are nondimensional Cartesian velocity vector, pressure, and temperature, respectively, and ξ is the random variable representing blowing ratio. The Cartesian coordinate is $\mathbf{x} = \{x_1, x_2, x_3\}$, where x_1, x_2, and x_3 are the streamwise, wall-normal, and spanwise directions, respectively, and the velocity vector is $\mathbf{u} = \{u_1, u_2, u_3\}$. Prandtl number is denoted by Pr and Reynolds number by Re defined as $\mathrm{Re} = U_\infty D/\nu$ with crossflow velocity, U_∞, and jet diameter, D, as the characteristic velocity and length scale, respectively. Temperature (T) is nondimensionalized using

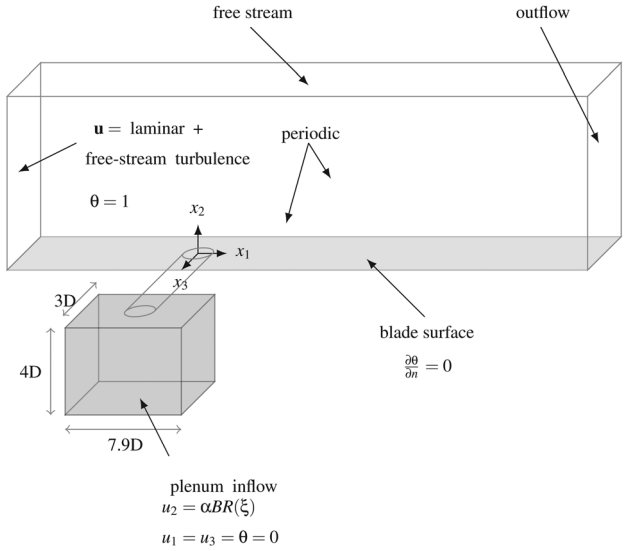

Fig. 1 Three-dimensional schematic of the jet in crossflow along with the boundary conditions

$$\theta(\mathbf{x}, t; \xi) = (T(\mathbf{x}, t; \xi) - T_c)/(T_h - T_c)$$

where T_h is the hot gas temperature and T_c is the coolant temperature.

The schematic of the domain and the boundary conditions used to solve Eqs. (1)–(3) are shown in Fig. 1. The origin of the coordinate system is at the center of the jet exit hole. The geometry includes a 35-deg delivery tube with diameter D and length of $3.5D$ originating from a plenum with the size of $7.9D \times 4D \times 3D$. The main domain, where the coolant and free-stream interact, spans the volume of $18D \times 6D \times 3D$ in streamwise, wall-normal, and spanwise directions, respectively. The center of the jet exit is located $6D$ downstream of the inlet boundary of the domain. For inflow boundary condition, a laminar boundary layer profile with the boundary layer thickness of $\delta_{99\%}/D = 1$ and temperature of $\theta = 1$ are used. The laminar boundary layer is superposed with free-stream turbulence that is generated by the spectral synthesizer method introduced in Ref. [21]. The free-stream turbulence is assumed to be isotropic with the intensity of 0.5% and length and time scale of $0.4D$ and $0.4D/U_\infty$, respectively. At the top boundary, free-stream condition is used with $\mathbf{u} = (U_\infty, 0, 0)$ and $\theta = 1$. At the outflow boundary, a zero-gradient condition is assumed for both velocity and temperature. In the spanwise direction, a periodic boundary condition is enforced, mimicking a situation where an array of holes are arranged in the spanwise direction with the center-to-center distance of $3D$. For all of the wall boundaries, a no-slip boundary condition for velocity and adiabatic boundary condition for temperature are used. The Reynolds number, $\mathrm{Re}_\infty = U_\infty D/\nu$, is 1500 throughout and the Prandtl number is $\mathrm{Pr} = 0.71$.

At the bottom of the plenum, a spatially-uniform random vertical velocity of $u_2 = \alpha \mathrm{BR}(\xi)$ is specified, where blowing ratio BR is the ratio of the space-averaged jet velocity in the delivery tube (U_j) to the crossflow velocity (U_∞) i.e., $\mathrm{BR} = U_j/U_\infty$, and α accounts for the area ratio of the bottom of the plenum (A_p) to the normal cross-sectional area of the delivery tube, i.e., $\alpha = \pi D^2/4A_p$. The area scaling factor for the current geometry is $\alpha = 0.0331$. The random blowing ratio, denoted by $\xi \equiv BR$, is characterized by symmetrically truncating the tails of a Gaussian distribution around its mean. Considering a Gaussian distribution with the probability density function (pdf) of

$$\rho(\xi) = \frac{1}{\sqrt{2\pi}\sigma}\exp(-(\xi - m)^2)/\sigma^2)$$

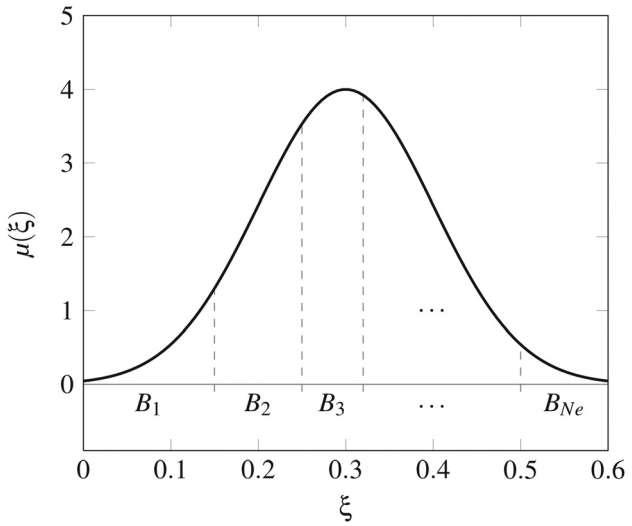

Fig. 2 Probability density function of blowing ratio; a truncated Gaussian distribution with mean of 0.3 and variance of 0.01. Elemental decomposition ($B_e, e = 1, \ldots, \mathrm{Ne}$) is shown schematically.

with mean of m and the standard deviation of σ, the pdf of the truncated Gaussian distribution is given by

$$\mu(\xi) = \begin{cases} \rho(\xi)/\beta, & |\xi - m| \le r, \\ 0, & \text{otherwise} \end{cases} \tag{4}$$

where β is the scaling factor to enforce that $\int_{\mathbb{R}} \mu(\xi)d\xi = 1$, and r is the distance from the mean beyond which $\rho(\xi)$ is truncated. Note that both pdf's, $\rho(\xi)$ and $\mu(\xi)$, have the same mean value of m, but their standard deviation values are different. In this study, we choose the mean value of $m = 0.3$, which is the blowing ratio at which the maximum film cooling effectiveness was observed according to the experimental/numerical measurements carried out by Bidan et al. [4] for a 35-deg inclined jet. The blowing ratio is allowed to have a range of variability in [0, 0.6], which amounts to 100% variation around its mean ($r = 0.3$). The standard deviation of the Gaussian distribution $\rho(\xi)$ is 0.1, which results in the standard deviation of $\sigma_{\mathrm{BR}} = 0.098$ for the truncated Gaussian distribution $\mu(\xi)$. The probability density function of the random blowing ratio is shown in Fig. 2.

It should be noted that in representing the variation or randomness in the blowing ratio, the notion of a temporal scale or time varying blowing ratio is not introduced here. Rather, it is assumed that the scale associated with the random variation is decoupled and much larger than the time scales associated with the turbulent flow fluctuations. This could indeed be the case in the engine application since the coolant is supplied from the compressor stage upstream, through its own separate plumbing system and its inherent system-dynamics.

Since adiabatic conditions are used at the surface $x_2 = 0$, the surface temperature field $\theta(\mathbf{x}, t; \xi)$ at $x_2 = 0$ represents a measure of the surface cooling effectiveness by the coolant film, which is defined by

$$\eta(x_1; \xi) = \frac{1}{w}\int_{-w/2}^{w/2} (1 - \bar{\theta}(\mathbf{x}; \xi))|_{x_2=0}\, dx_3 \tag{5}$$

where $\eta(x_1; \xi)$ is the spanwise-averaged film cooling effectiveness, w is the width of the cooled surface and the operator $\overline{(.)}$ represents a time-averaged quantity. Variations in blowing ratio (ξ) will lead to variations in temperature and Eq. (5) can be used to quantify this effect on film cooling effectiveness $\eta(x_1; \xi)$.

Further, a spatially-averaged (overall) film cooling effectiveness, denoted by $\tilde{\eta}(\xi)$, can be obtained from

$$\tilde{\eta}(\xi) = \frac{1}{x_{1_e} - x_{1_s}}\int_{x_{1_s}}^{x_{1_e}} \eta(x_1; \xi)dx_1 \tag{6}$$

where x_{1_s} and x_{1_e} denote the beginning and the end of the streamwise interval over which $\tilde{\eta}(\xi)$ is calculated. In this study, $x_{1_s} = 1$ and $x_{1_e} = 12$.

The objective of the current work is to investigate the effect of uncertainty of blowing ratio represented by the pdf shown in Fig. 2 on the measures of the film cooling effectiveness, $\eta(x_1; \xi)$ and $\tilde{\eta}(\xi)$, and the representative statistics associated with these measures.

3 Numerical Algorithm

As it was demonstrated in Sec. 2, blowing ratio is a random number and adds another dimension, which is referred to as *parametric space*, to the governing equations. Note that solving the film cooling problem given by Eqs. (1)–(3) for a constant deterministic blowing ratio requires performing a DNS simulation with several millions degree of freedom. Therefore adding another dimension requires an efficient discretization strategy to solve an already expensive problem. In this section, we explain the numerical algorithm that is used in the current study to solve Eqs. (1)–(3).

3.1 Stochastic Discretization

3.1.1 Decomposition in Parametric Space. We use ME-gPC introduced by Wan and Karniadakis [12] to discretize governing Eqs. (1)–(3) in the one-dimensional parametric space, which is formed by the random blowing ratio in the range of $B = [0, 0.6]$. We first decompose the parametric space B into Ne nonoverlapping elements denoted by: $B_1, B_2, B_3, \ldots, B_{\mathrm{Ne}}$. Note that each element B_e is a segment of the blowing ratio interval [0, 0.6], and

$$B_e = [a_e, b_e)$$

where a_e and b_e are the beginning and the end of element B_e, respectively, and since the elements are non-overlapping, the end of one element is the beginning of the next element, i.e., $b_e = a_{e+1}$. The schematic of this decomposition is shown in Fig. 2. We introduce the indicator random variable

$$I_{B_e}(\xi) = \begin{cases} 1, & \xi \text{ belongs to } B_e, \\ 0, & \text{otherwise} \end{cases} \tag{7}$$

If a sample of blowing ratio, ξ, with the pdf given by Eq. (4), is drawn and the sample resides in the element B_e, the value of $I_{B_e}(\xi)$ is one and if the sample resides outside of the element B_e, the value of $I_{B_e}(\xi)$ is zero. From the law of total probability, we have

$$\Pr(\xi \le q) = \sum_{e=1}^{\mathrm{Ne}} \Pr(\xi \le q | I_{B_e} = 1)\Pr(I_{B_e} = 1) \tag{8}$$

where $\Pr(\mathcal{E})$ is the probability of event $\mathcal{E}$, and $\Pr(\mathcal{E}|\mathcal{F})$ is the conditional probability and represents the probability of event $\mathcal{E}$ given that event $\mathcal{F}$ has occurred. Also note that from the definition of the indicator random variable given by Eq. (7), we arrive at

$$\Pr(I_{B_e} = 1) = \int_{B_e} \mu(\xi)d\xi$$

Now using Bayes' rule, we have

$$\hat{\mu}_e(\xi|I_{B_e}=1)=\frac{\mu(\xi)}{\Pr(I_{B_e}=1)} \tag{9}$$

where $\hat{\mu}_e(\xi|I_{B_e}=1)$ is the conditional pdf with the condition of $I_{B_e}=1$, which, by using Eq. (7), can be interpreted as: *if the random variable ξ resides in the element B_e*. The expectation of a generic function $f(\xi)$ in the global domain B is obtained by

$$\mathbb{E}(f(\xi))=\int_B f(\xi)\mu(\xi)d\xi \tag{10}$$

Using Eqs. (8)–(10), we reach at

$$\mathbb{E}[f(\xi)]=\sum_{e=1}^{\mathrm{Ne}}\Pr(I_{B_e}=1)\int_{B_e} f(\xi)\hat{\mu}_e(\xi|I_{B_e}=1)d\xi \tag{11}$$

Above equation provides a basis for the calculation of statistical information from the elemental to the global level. The definition of the expectation motivates a natural weighted inner product with pdf as the weight. This follows:

$$(f,g)_\mu:=\mathbb{E}[f(\xi)g(\xi)],\quad ||f||_\mu:=(f,f)_\mu^{1/2} \tag{12}$$

where $(.,.)_\mu$ is the inner product and $||.||_\mu$ is the norm with respect to the weight $\mu(\xi)$. Thus for two random functions of $f(\xi)$ and $g(\xi)$, the condition of $(f,g)_\mu=0$ indicates orthogonality; a concept that is used in Sec. 3.1.2 to define an orthogonal basis for expansion of a generic function.

3.1.2 Stochastic Collocation. We consider a basis consisting of local polynomial chaos up to order M in each element B_e which are denoted by $\phi_i^e(\xi)$, where $i=0,1,\ldots,M$ is the polynomial order and $e=1,2,\ldots,Ne$ denotes the element number. A zero extension of polynomial $\phi_i^e(\xi)$ in region outside the element B_e is assumed, i.e.,

$$\phi_i^e(\xi)=0,\qquad \xi \quad \text{outside of } B_e.$$

The polynomials $\phi_i^e(\xi)$ for $i=0,\ldots,M$ are mutually orthogonal with respect to the local pdf of $\hat{\mu}_e(\xi)$. In other words

$$\int_{B_e}\phi_i^e(\xi)\phi_j^e(\xi)\hat{\mu}_e(\xi|I_{B_e}=1)d\xi=(\gamma_i^e)^2\delta_{ij} \tag{13}$$

where γ_i^e is the norm of the polynomial $\phi_i^e(\xi)$ and is given by

$$(\gamma_i^e)^2=\int_{B_e}\phi_i^e(\xi)^2\hat{\mu}_e(\xi|I_{B_e}=1)d\xi \tag{14}$$

These polynomials are constructed numerically using the procedure proposed by Wan and Karniadakis [12]. The polynomials $\phi_i^e(\xi)$ with $i=0,1,2,\ldots$, form a hierarchical basis. Note that by considering the zero expansion of polynomial $\phi_i^e(\xi)$ outside of the element B_e, orthogonality in the global sense is also retained, i.e.,

$$\mathbb{E}[\phi_i^e(\xi)\phi_j^e(\xi)]=\Pr(I_{B_e}=1)(\gamma_i^e)^2\delta_{ij} \tag{15}$$

Now, we consider a polynomial expansion for time-averaged temperature, denoted by $\bar{\theta}$, as follows:

$$\bar{\theta}_M(\mathbf{x};\xi)=\sum_{e=1}^{\mathrm{Ne}}\sum_{k=0}^{M}\hat{\bar{\theta}}_k^e(\mathbf{x})\phi_k^e(\xi) \tag{16}$$

where the subscript M represents the projection of the respective field onto to the polynomial basis $\phi_i^e(\xi)$, and $\widehat{\overline{\mathbf{u}}}_k^e(\mathbf{x})$, $\hat{\bar{p}}_k^e(\mathbf{x})$, and $\hat{\bar{\theta}}_k^e(\mathbf{x})$ are the expansion coefficients. In the remaining of this section, in the interest of brevity, we carry out the formulation for temperature only, noting that the procedure can be similarly replicated for time-averaged velocity and pressure. The expansion coefficients $\hat{\bar{\theta}}_k^e(\mathbf{x})$ are obtained by employing Galerkin projection. This follows:

$$\hat{\bar{\theta}}_k^e(\mathbf{x})=\mathbb{E}[\bar{\theta}_M(\mathbf{x};\xi)\phi_k^e(\xi)]/\mathbb{E}[\phi_k^e(\xi)^2],\quad 0\le k\le M,\quad 1\le e\le \mathrm{Ne} \tag{17}$$

To estimate the coefficient $\widehat{\overline{\mathbf{u}}}_k^e(\mathbf{x})$, we use pseudo-spectral projection method [22] by using Gauss-quadrature rule which for a generic function f is defined as

$$\int_{B_e} f(\xi)\hat{\mu}_e(\xi|I_{B_e}=1)d\xi\simeq\sum_{i=0}^{Q}w_{(i)}^e f(\mathbf{x};\xi_{(i)}^e) \tag{18}$$

where $\{\xi_{(i)}^e,w_{(i)}^e\}_{i=0}^Q$ are a set of $Q+1$ Gauss-quadrature points and weights in element B_e. Note that the $(Q+1)$-point Gauss quadrature formula is exact to evaluate $\mathbb{E}[f]$ for any polynomial f up to degree $2Q+1$. By using the quadrature rule given by Eqs. (18) and (14), the expansion coefficients for temperature given by Eq. (17) can be estimated as

$$\hat{\bar{\theta}}_k^e(\mathbf{x})\simeq\sum_{i=0}^{Q}w_{(i)}^e\theta(\mathbf{x};\xi_{(i)}^e)\phi_k^e(\xi_{(i)}^e)/\gamma_k^{e^2},\quad 0\le k\le M,\quad 1\le e\le \mathrm{Ne} \tag{19}$$

By replacing above equation in the polynomial expansion given by Eq. (16), a low-dimensional representation of random temperature is obtained which can serve as an off-line *stochastic surrogate model* whose evaluation is inexpensive.

3.1.3 Cost-Effectiveness and Numerical Efficiency. To show the efficiency of the current approach let's consider the error of the expansion $f_M(\xi)=\sum_{e=1}^{\mathrm{Ne}}\sum_{k=0}^{M}\hat{f}_k^e\phi_k^e(\xi)$ as

$$\varepsilon^2=\mathbb{E}[(f(\xi)-f_M(\xi))^2]=\int_{B_e}(f(\xi)-f_M(\xi))^2\mu(\xi)d\xi \tag{20}$$

where $f(\xi)$ represents the exact solution and $f_M(\xi)$ represents the orthogonal projection of $f(\xi)$ onto polynomial space up to order M similar to Eq. (16). The discretization discussed in Secs. 3.1.1 and 3.1.2 with only one element, i.e., $\mathrm{Ne}\equiv 1$, represents the gPC discretization of the random space which has the following characteristics:

(1) If $f(\xi)$ is a smooth function of ξ, i.e., infinitely differentiable, $f_M(\xi)$ converges *exponentially fast* to $f(\xi)$ as M increases. The assumption of smoothness of film cooling effectiveness as a function of blowing ratio is later confirmed in Sec. 4.3, where the fast convergence of $\tilde{\eta}_M(\xi)$ is observed in Fig. 8. Moreover, since the coefficients of $f_M(\xi)$, $\hat{f}_k^e$, are obtained using the Galerkin projection, (which is an *orthogonal projection*), analogous to Eq. (17), $f_M(\xi)$ is the best approximation among any other polynomial expansion up to order M. More specifically, this means that the expansion error, ε, given by Eq. (20), is minimum among all polynomial expansions up to order M of $f(\xi)$ (see Ref. [23], chapter 3 for more details).
(2) Since the expansion basis is orthogonal, the coefficients of the polynomial expansion can be effectively computed using Gauss quadrature points and weights in the quadrature rule.
(3) Since a stochastic collocation approach is used, all deterministic simulations can run concurrently and independently.

The above observations are at the core of the cost-effectiveness and efficiency of the gPC expansion. In fact, fast convergence of the gPC expansion to the exact solution reduces the polynomial order M required to reach a desired level of accuracy $\varepsilon := \varepsilon_{\text{des}}$, when compared to low-order methods. Note that the polynomial order M is directly equivalent to the computational cost, since for an expansion with polynomial order M and one element, $M+1$ deterministic simulations need to be performed. In this study, we employ ME-gPC where we use several elements to discretize the parametric space. This strategy improves the accuracy of the method in cases where function $f(\xi)$ does not have enough smoothness, while maintaining the computational advantages as stated above (see Ref. [11,12] for more discussion).

3.1.4 Statistical Information. The stochastic surrogate model given by Eq. (19) can be used to calculate the statistical moments such as expectation using

$$\mathbb{E}[\bar{\theta}_M(\mathbf{x};\xi)] = \sum_{e=1}^{Ne}\sum_{k=0}^{M} \hat{\bar{\theta}}_k^e(\mathbf{x})\mathbb{E}[\phi_k^e(\xi)] \tag{21}$$

and by considering the orthogonality of the basis (Eq. (15)), the variance is calculated from

$$\sigma_\theta^2(\mathbf{x}) = \sum_{e=1}^{\text{Ne}}\sum_{k=0}^{M} \hat{\bar{\theta}}_k^e(\mathbf{x})^2\mathbb{E}[\phi_k^e(\xi)^2] - \sum_{e=1}^{Ne}\sum_{k=0}^{M} \hat{\bar{\theta}}_k^e(\mathbf{x})^2\mathbb{E}[\phi_k^e(\xi)]^2 \tag{22}$$

where $\sigma_\theta(\mathbf{x})$ is the standard deviation of the temperature at point $\mathbf{x}$ in space. The expansion for temperature given by Eq. (16) can accordingly be used to calculate the statistical moments for spanwise-averaged film cooling effectiveness, $\eta(x_1;\ \xi)$, and spatially-averaged film cooling effectiveness, $\tilde{\eta}(\xi)$, by using Eqs. (5) and (6), respectively.

Another useful statistical information that can be extracted is the *sensitivity* of time-averaged quantities with respect to the random blowing ratio, which, for instance, for temperature is defined as

$$\mathcal{S}_\theta(\mathbf{x}) = \mathbb{E}\left[\frac{\partial\bar{\theta}_M(\mathbf{x};\xi)}{\partial\xi}\right] = \sum_{e=1}^{\text{Ne}}\sum_{k=0}^{M} \hat{\bar{\theta}}_k^e(\mathbf{x})\mathbb{E}\left[\frac{\partial\phi_k^e(\xi)}{\partial\xi}\right] \tag{23}$$

where $\mathcal{S}_\theta(\mathbf{x})$ denotes the sensitivity of time-averaged temperature with respect to random variation of blowing ratio.

Note that using Eq. (5), the expectation, variance and sensitivity for spanwise-averaged film cooling effectiveness become

$$\mathbb{E}[\eta(x_1;\xi)] = \frac{1}{w}\int_{-w/2}^{w/2}(1-\mathbb{E}[\bar{\theta}_M(\mathbf{x};\xi)])|_{x_2=0}\,dx_3 \tag{24}$$

$$\sigma_\eta^2(x_1) = \frac{1}{w}\int_{-w/2}^{w/2}\sigma_\theta^2(\mathbf{x})|_{x_2=0}\,dx_3 \tag{25}$$

$$\mathcal{S}_\eta(x_1) = \frac{1}{w}\int_{-w/2}^{w/2}\mathcal{S}_\theta(\mathbf{x})|_{x_2=0}\,dx_3 \tag{26}$$

3.1.5 Discretization Details. In the current study, we use five elements, i.e., Ne = 5. The beginning the intervals are $a_1 = 0.00$, $a_2 = 0.05$, $a_3 = 0.15$, $a_4 = 0.30$, and $a_5 = 0.45$, and the end of the intervals are $b_1 = 0.05$, $b_2 = 0.15$, $b_3 = 0.30$, $b_4 = 0.45$, and $b_5 = 0.60$, providing a set of nonoverlapping elements that covers BR in the range of [0, 0.6]. The elements are refined at BR = 0, where BR = 0 represents the condition that the jet is off. By increasing blowing ratio from zero large gradients of velocity, pressure, and temperature are expected, which implies that local refinement may be necessary. This is consistent with the properties of the ME-gPC method where a local-refinement strategy can be adopted by either increasing the polynomial order locally (known as $p-$refinement), or refining the element size (known as $h-$refinement); the later of which is adopted in this study. On the other hand, in gPC method, increasing the polynomial order globally is the only refinement strategy which may not be efficient if low regularity or sharp transition exists locally.

We choose polynomial order $M = 3$ within each element. Note that the polynomial basis is orthogonal with respect to the local pdf of $\hat{\mu}_e(\xi|I_{B_e} = 1)$ in each element and as a result the polynomial bases of the same degree are different from one element to another. We use 4 Gauss quadrature points ($Q = 3$) which results in a degree of exactness of $2Q+1 = 7$, when evaluating $\mathbb{E}[f]$ in each element. In total, $\text{Ne} \times (Q+1)$ times sampling of the governing Eqs. (1)–(3) is required. Therefore for the given parameters, 20 DNS simulations are performed.

3.2 Discretization in Space and Time. In all the cases in this study, we perform direct numerical simulation on the jet in crossflow with the schematic of the problem shown in Fig. 1. For discretization in space, we use spectral element method with hexahedral element implemented in $\mathcal{N}\varepsilon\kappa\mathcal{T}\alpha r$ [24]. A third-order semi-implicit fractional step method is used to advance the governing equations in time. For more details on the method and its implementation see Ref. [25].

A three-dimensional view of the computational grid that is used in this study is shown in Fig. 3(*a*). To generate the grid, a total number of 2226 quadrilateral elements were first generated in $x_1 - x_3$ plane at the jet exit elevation, out of which 372 elements belonged to the jet exit. A closer view of this grid near the jet exit is shown in Fig. 3(*b*). The two-dimensional grid was then swept along the x_2 direction generating 17 parallel layers of grid with increasing height away from the wall. The first-layer elements have a height of $\Delta x_2 = 0.05D$ and large elements with the height of $3D$ were used for the topmost layer. Similarly, within the pipe the grid at the jet exit was swept with 24 layers along the axis of the tube with the height of $\Delta x_2 = 0.07D$ for the first and last layer. An analogous strategy to that of the main domain was used for generating grid in the plenum where first a quadrilateral grid with 720 elements were generated at the top $x_1 - x_3$ plane. These elements were then swept downward to the plenum inlet creating 11 layers with $\Delta x_2 = 0.06D$ at the topmost layer and $\Delta x_2 = 1.2D$ at the bottommost layer. The final grid obtained had 52464 elements. We use polynomial with spectral order of four which translates into $(4+1)^3 = 125$ points within each element, resulting in approximately a total of 6.5 millions points. The same grid is used in all simulations and the grid spacing in the wall coordinate $x_i^+ = u_\tau x_i/\nu$, where $u_\tau = \sqrt{\nu(\partial u_1/\partial x_2)_{\text{wall}}}$ is the average friction velocity for the highest blowing ratio (BR = 0.5841), is related to the regular spacing by $\Delta x_i^+ = 375\Delta x_i$. Given that polynomial with spectral order of four is used within each element, the accuracy is comparable with Fourier spectral method with two complete modes resolved in each element. On the other hand, a finite difference approximation would require 5 points to capture two complete Fourier modes. Therefore, the resolution in the wall-normal direction of the first-layer element in the main domain in a finite difference spirit is $\Delta x_2^+ = 0.05 \times 375/4 = 4.69$. However note that the spectral element with polynomial order of P is significantly more accurate than a $(P+1)$-point-finite-difference approximation. For a more detailed discussion on this see Ref. [25]. In the same way, the resolution of the grid in the main domain in the streamwise direction is $7.5 \le \Delta x_1^+ \le 20$ and in the spanwise direction $7.5 \le \Delta x_3^+ \le 14$.

The spectrum of the kinetic energy $E = (u_1^2 + u_2^2 + u_3^2)^{1/2}/2$ at point $x_1 = 2$, $x_2 = 1$, and $x_3 = 0$ for the highest blowing ratio considered in this study is shown in Fig. 4. The Kolmogorov inertial range with the slope of $-5/3$ is observed.

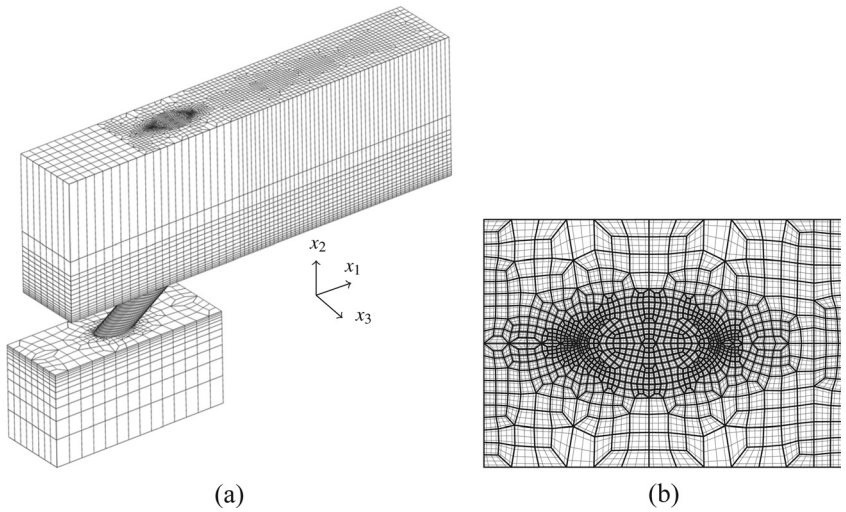

Fig. 3 Unstructured hexahedral grid; (*a*) three-dimensional view; (*b*) $x_1 - x_3$ view of the grid in the vicinity of the jet exit, black lines: element boundaries; gray lines: Gauss-Lobatto-Legendre quadrature grid with spectral order of four

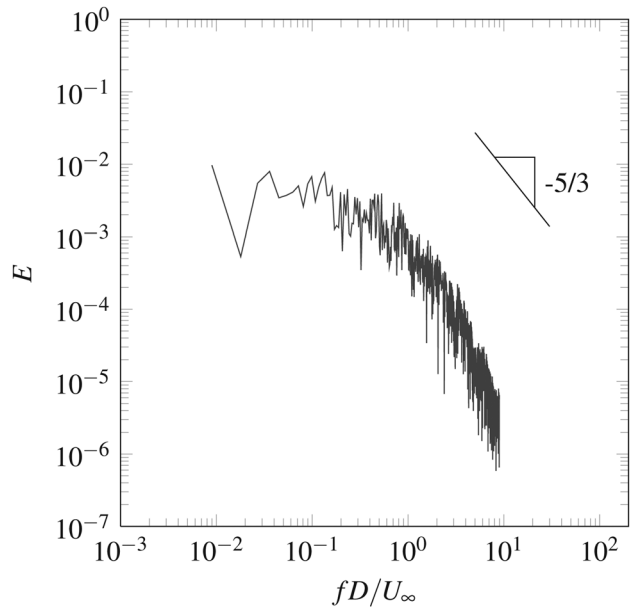

Fig. 4 Spectrum of the energy of the velocity signal at location $x_1 = 2$, $x_2 = 1$, and $x_3 = 0$ with blowing ratio of BR = 0.5841

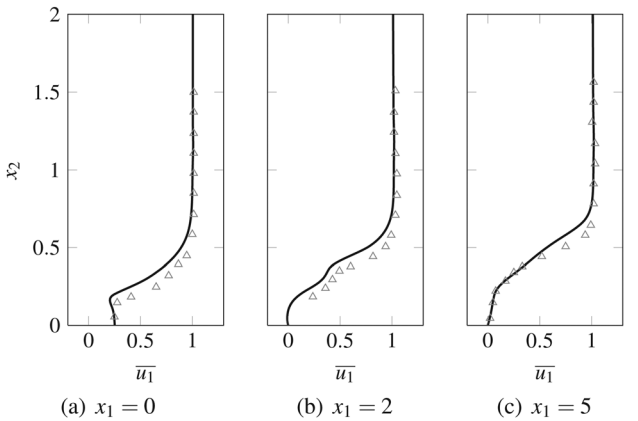

Fig. 5 Time-averaged streamwise velocity profiles $\overline{u_1}$ at $x_2 = 0$ and BR = 0.15; DNS (solid line), experimental data [4] (triangle)

4 Results

4.1 Comparison With Experiment. In this section, we compare the numerical results obtained from the DNS with experimental measurements performed by Bidan et al. [4]. The geometry includes a 35-deg inclined pipe with the diameter of D and length of $7D$. The main domain spans the volume of $21D \times 10D \times 6D$ in steamwise, wall-normal, and spanwise directions, respectively. The inflow boundary condition is a laminar boundary layer with the thickness of $\delta = 0.63D$. The experimental setup does not have a plenum and the jet inflow boundary condition is enforced at the pipe inlet, where a uniform flow is superposed with 10% turbulence, generated by employing the spectral synthesizer method introduced in Ref. [21]. The Reynolds number based on the freestream velocity and the jet diameter is $\mathrm{Re}_\infty = U_\infty \delta/\nu = 1710$. A hexahedral grid with 121,700 elements with a spectral order of four was used. In Fig. 5, the profiles of time-averaged streamwise velocity are compared with those of experimental measurements in Ref. [4] at three different streamwise sections on the centerline plane. The agreement between the predictions and the measured data is good, which gives us greater confidence in carrying out the computations with the current approach.

4.2 Effect of Blowing Ratio on Film Cooling. We performed twenty direct numerical simulations in total, at Gauss-quadrature points in the parametric space, where each quadrature point represents a unique blowing ratio. For each simulation, time-averaged quantities are collected and used in Eq. (19) to compute the expansion coefficients. Finally, the stochastic response of the system is constructed using Eq. (16) from which all the statistical information can be directly extracted.

Figure 6 shows the instantaneous temperature field at the midplane ($x_3 = 0$) at six quadrature points in the parametric space. At BR = 0.004, a significant ingestion of the crossflow gas into the delivery tube can be seen. As the blowing ratio increases (BR = 0.1442), the coverage extends to a larger portion of the surface downstream of the jet, improving the spatially-averaged film cooling effectiveness. This trend continues up to BR = 0.2902 where the shear layer tends to become unstable around $x_1 = 6$ as evidenced by the unsteadiness in the time sequence of the data. At BR = 0.3956, a clear roll-up of the shear layer can be seen which leads to the formation of hairpin vortices that shed periodically

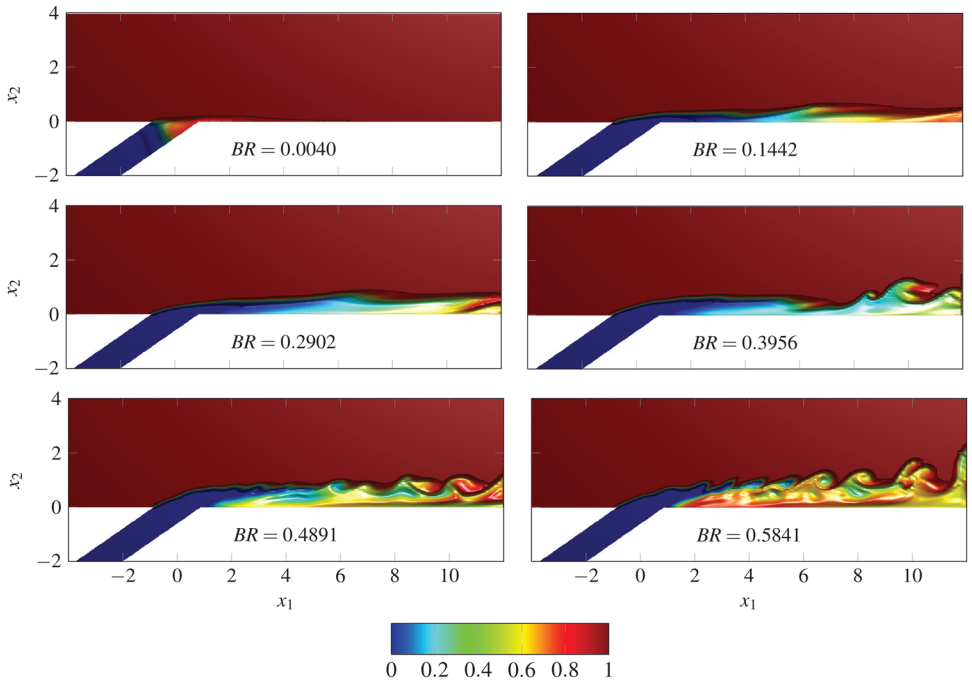

Fig. 6 Instantaneous temperature surface in the mid-plane ($x_3 = 0$) for different blowing ratios

after $x_1 \geq 6$. As blowing ratio further increases, the coolant jet detaches from the surface, leading to the reduction of the coverage in the near-hole region. At BR = 0.4891, the roll-up of the shear layer occurs closer to the hole and due to the separation of the coolant from the surface, film cooling effectiveness continues to decrease. At BR = 0.5841, the jet is fully detached and the cross-flow then penetrates in the region behind the jet body and causes a poor coverage of the surface.

Figure 7 shows the time-averaged temperature on the cooled surface for all quadrature points. It is clear that as blowing ratio increases from the small value of BR = 0.004 to BR = 0.2044, the film cooling effectiveness improves everywhere on the surface. However further increase in blowing ratio (BR = 0.2538) results in reduction of the film cooling effectiveness in the vicinity of the jet exit due to the jet liftoff, but further downstream ($x_1 > 5$) the effectiveness still increases, which is caused by the re-attachment of the coolant jet. The spanwise coverage also increases modestly up to higher blowing ratios (BR $\geq$ 0.4891), after which the deterioration of the coverage is more pronounced immediately downstream of the jet exit ($x_1 < 2$) and less strongly further downstream ($x_1 > 5$).

4.3 Spatially-Averaged Film Cooling Effectiveness. The previous observations from Figs. 6 and 7 indicate that an optimal blowing ratio exists. In Fig. 8, the spatially-averaged film cooling effectiveness, $\bar{\eta}(\xi)$, versus blowing ratio is shown. The optimal blowing ratio is approximately at $\mathrm{BR}_{\mathrm{opt}} = 0.3$, which is in agreement with the experimental/numerical study carried out by Bidan et al. [4]. The projections of $\bar{\eta}(\xi)$ to different polynomial orders ranging from $M = 0$ to $M = 3$ are also shown in Fig. 8. The response surface with projection order of $M = 0$ represents a piece-wise constant approximation of the response surface, whose computation cost is equivalent to five deterministic direct numerical simulations. As it is clear, this approximation provides a rough measure of the response surface and relatively large amount of error would be associated with statistical quantities computed from this approximation. However as polynomial order increases

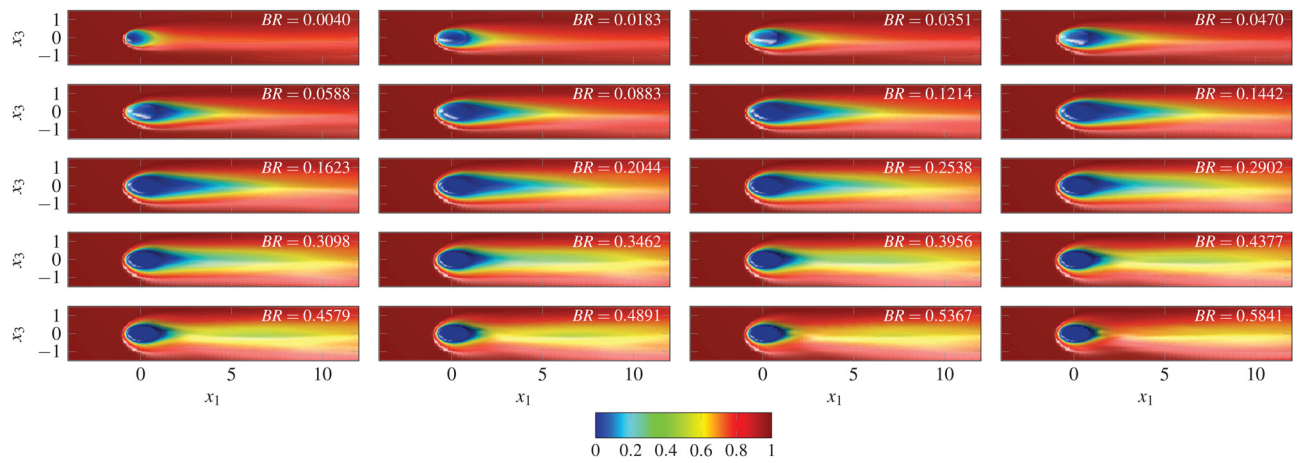

Fig. 7 Time-averaged temperature contours for quadrature points on cooled surface ($x_2 = 0$). In this figure simulations for all Gauss quadrature points are shown.

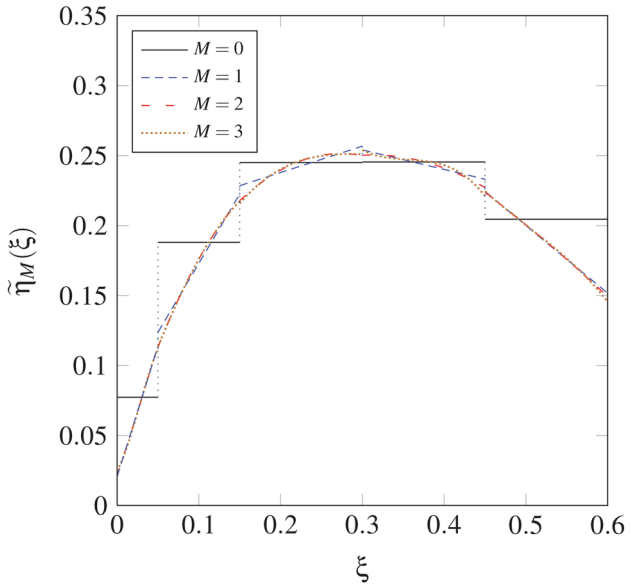

Fig. 8 Spatially-averaged film cooling effectiveness $\tilde{\eta}_M(\xi)$ with different projection orders $M = 0, \ldots, 3$

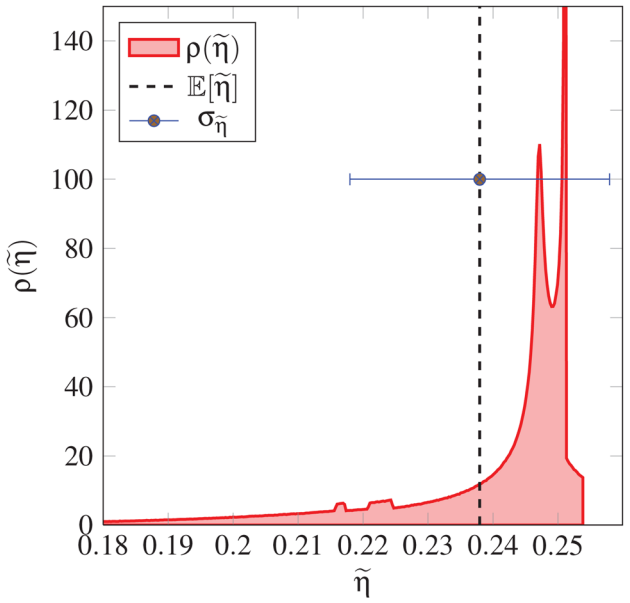

Fig. 9 Probability density function for film cooling effectiveness $\tilde{\eta}(\xi)$

to $M = 1$ (piece-wise linear) the approximation significantly improves. The improvement of the response surface continues as projection order increases to $M = 2$ and the difference between the response surfaces with projection orders of $M = 2$ and $M = 3$, as it can be seen in Fig. 8, is negligible.

An important requirement for ME-gPC to be a numerically efficient approach is that $\tilde{\eta}(\xi)$ must be a piece-wise smooth function of ξ. The fast convergence of $\tilde{\eta}_M(\xi)$ with increasing projection order from $M = 0$ to $M = 3$ can be qualitatively observed in Fig. 8 that assures that $\tilde{\eta}(\xi)$ is in fact a piece-wise smooth function of ξ. This important numerical observation shows that ME-gPC is an efficient numerical method in investigating the effect of uncertainty of blowing ratio on film cooling effectiveness. The decision on what order of projection order is suitable depends on what level of accuracy is desired. However, in any circumstances, if only a certain number of DNS runs can be afforded, it is still better to perform those simulations in the current framework, since according to the statements made in Sec. 3.1.3, for the current elemental decomposition, the response surface with projection order $M = 0$, for instance, is the best response surface among all piecewise constant response surfaces (see Sec. 3.1.3 for the error definition). The similar statements can be made for response surfaces with projection orders $M = 1$, 2, and 3.

Note that the polynomial $\phi_i^e(\xi)$ are discontinuous across elements, however the discontinuity at the element interfaces is of measure zero (i.e., negligible) with respect to the norm given by Eq. (12). One could have chosen Gauss-Lobatto-Legendre quadrature points where the end points of the elements are included and thus the continuity across the elements is ensured, however, in that case the degree of exactness for $(Q + 1)$ quadrature points is $2Q - 1$ as opposed to the degree of exactness of $2Q + 1$ for the Gauss quadrature points used in this study, resulting in larger amount of error overall for the Gauss-Lobatto-Legendre quadrature points. Nevertheless for a fixed elemental decomposition, the current choice of quadrature points gives the best polynomial approximation when the error is measured in the norm given by Eq. (12). For a more detailed discussion in this regard see Ref. [12].

Mathematically, the relationship between the pdf of the random blowing ratio $\mu(\xi)$ and the pdf of film cooling effectiveness $\rho(\eta)$ is determined by

$$\rho(\eta) = \mu(\xi)/|(d\eta/d\xi)| \tag{27}$$

where we assume that $\eta(\xi)$ is monotonic for simplicity. Equation (27) has two implications:

(1) The existence of regions in which blowing ratio has high probability of occurrence, increases the likelihood of the film cooling effectiveness occurrence at values of $\eta(\xi)$ associated with those blowing ratios.
(2) The pdf of the film cooling effectiveness, $\rho(\eta)$, is inversely proportional to the slope of η versus ξ. In other words, the regions where film cooling effectiveness is not *sensitive* to the variation of blowing ratio, i.e., low $d\eta/d\xi$, tend to increase the likelihood of occurrence of values of η corresponding to those blowing ratios.

As it is clear from Fig. 8, $\tilde{\eta}(\xi)$ is not a monotonic function of ξ, and therefore Eq. (27) cannot be used to calculate the pdf of $\tilde{\eta}(\xi)$. Instead, we use Monte Carlo method where ξ is sampled from its distribution, the truncated Gaussian $\mu(\xi)$ with the mean of 0.3 and standard deviation of $\sigma_{BR} = 0.098$. This is achieved by first drawing samples from Gaussian distribution $\rho(\xi)$ with the mean of 0.3 and the standard deviation of 0.1. Then, the samples (ξ's) that are outside the region of [0, 0.6], are rejected. We draw twenty million samples from ξ's distribution. Negligible difference between the histogram of the samples and the exact pdf was observed, indicating that the sample size is sufficiently large. Next, $\tilde{\eta}(\xi)$ is evaluated at all sampled ξ's, creating a collection of twenty million samples of $\tilde{\eta}(\xi)$, whose pdf is shown in Fig. 9. Note that sampling from the ξ's distribution and evaluating $\tilde{\eta}(\xi)$ at these samples are carried out as post processing and it takes only seconds to perform the calculations. The maximum value of $\tilde{\eta}(\xi)$ is 0.254 and all other values for $\tilde{\eta}(\xi)$ are below this peak number. Therefore, the probability of $\tilde{\eta}(\xi)$ beyond this peak is zero, which is reflected by the sudden drop of the value of $\rho(\tilde{\eta})$ to zero for $\tilde{\eta}(\xi) > 0.254$. The value of $\rho(\tilde{\eta})$ becomes unbounded at $\tilde{\eta} = 0.251$, since $d\tilde{\eta}/d\xi = 0$ at this point. There is a second smaller peak at $\tilde{\eta}$ of 0.246, which is related to the near-zero slope of $\tilde{\eta}(\xi)$ at this value as shown in Fig. 9. Two square-shape jumps in the profile of $\rho(\tilde{\eta})$ in the region of $0.215 < \tilde{\eta} < 0.225$ are triggered by the small discontinuity of $\tilde{\eta}(\xi)$ at elemental boundaries (discussed in the preceding paragraph).

Once the film cooling effectiveness response is obtained all statistical moments can be computed. The expected value for the spatially-averaged film cooling effectiveness is $\mathbb{E}[\tilde{\eta}] = 0.238$ and is shown by a vertical dashed line in Fig. 9. It is important to note

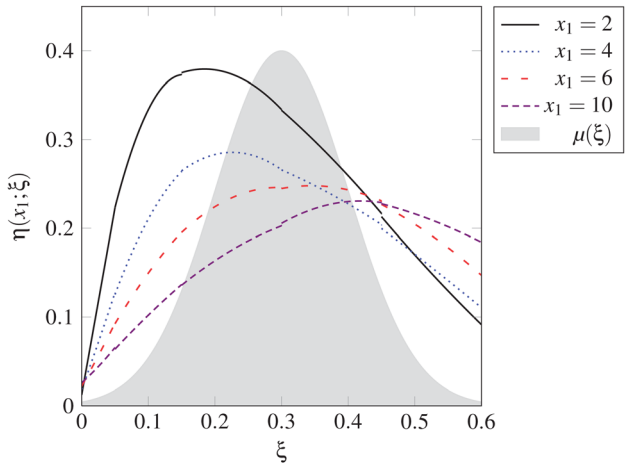

Fig. 10 Spanwise-averaged film cooling effectiveness $\eta(x_1; \xi)$ versus random blowing ratio at $x_1 = 2$, 4, 6, and 10

that this expected value is lower than the optimal value of effectiveness of 0.25 at the design BR of 0.3. This deterioration in cooling performance is not surprising since it is linked to the variation in the blowing ratio around the 0.3 value, and cooling performance worsens on either side of the 0.3 value. The standard deviation of the spatially-averaged film cooling effectiveness is $\sigma_{\bar{\eta}} = 0.022$ which is equivalent to $\pm 9.4\%$ variation with respect to the expected value. This implies an overall cooling effectiveness range of 0.216–0.26. In view of the blowing ratio variations that are naturally present in the gas turbine environment, the expected value $\mathbb{E}[\bar{\eta}]$ and the range of the cooling effectiveness around $\mathbb{E}[\bar{\eta}]$ are of significant value to the turbine designer because it allows for the incorporation of realistic effects such as the blowing ratio variations.

4.4 Spanwise-Averaged Film Cooling Effectiveness. In Fig. 10, the spanwise-averaged film cooling effectiveness at four streamwise stations are shown. The film cooling effectiveness at $x_1 = 2$ increases from BR = 0 and reaches the maximum of $\eta = 0.38$ at BR = 0.18. Further increase in blowing ratio leads to the jet liftoff and a decrease in η is observed. The slope $d\eta/d\xi$ decreases as the maximum η value is reached which according to Eq. (27), causes the sharp increase of $\rho(\eta)$ as it is shown in Fig. 11(*a*). At the maximum of η ($\eta = 0.38$), $d\eta/d\xi = 0$, and therefore $\rho(\eta)$ becomes unbounded. As the blowing ratio increases, the magnitude of slope of $\eta(\xi)$ increases as well, which contributes to the decrease in $\rho(\eta)$. However, the likelihood of blowing ratio residing in this region increases (large $\mu(\xi)$) which prohibits a fast decay of $\rho(\eta)$. As a result a relatively large spread of $\rho(\eta)$ around its mean is observed, which is responsible for large values of the standard deviation. Physically, large amount of the standard deviation implies significant fluctuations in the cooling effectiveness values despite the high cooling effectiveness values of 0.38 at this region. This is further illustrated in Fig. 12, where at $x_1 = 2$, the expected value $\mathbb{E}[\bar{\eta}] = 0.316$ and the standard deviation is 0.058. At $x_1 = 4$ the maximum of η occurs at higher blowing ratio of BR = 0.23. This overlap of the low-slope region near the η-maximum with the region of high probability for blowing ratio tends to centralize $\rho(\eta)$ in the overlapped region and thus it decreases the spread of the pdf as it is shown in Fig. 11(*b*). As a consequence the variance at this x_1 decreases. This trend continues up to $x_1 = 6$, where the width of the low-slope region widens and also the maximum of η nearly coincides with the maximum of $\mu(\xi)$ at $\xi = 0.3$. This gives rise to the most concentrated $\rho(\eta)$ among the four cases considered here, as it is shown in Fig. 11(*c*), and therefore the least amount of the standard deviation is observed at $x_1 = 6$. This implies that at this downstream location, despite the variability in the upstream BR, its impact on the cooling effectiveness

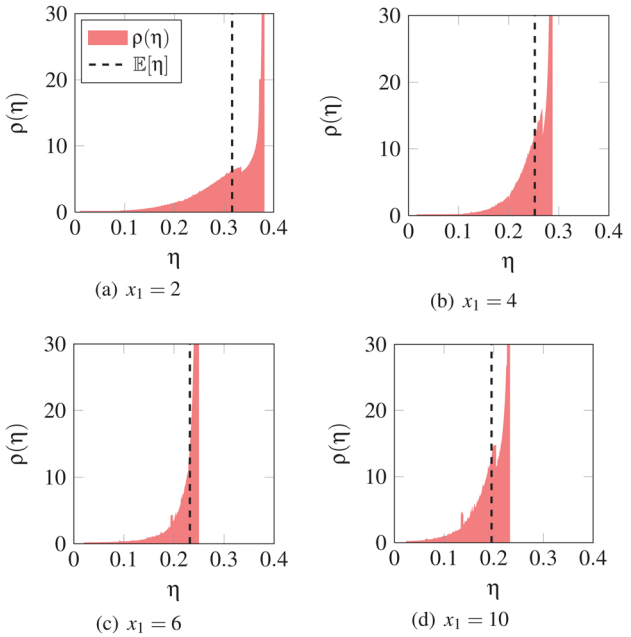

Fig. 11 The pdf of spanwise-averaged film cooling effectiveness at $x_1 = 2$, 4, 6, and 10. Note that the horizontal axis in (*a*)–(*d*) corresponds to the vertical axis in Fig. 10.

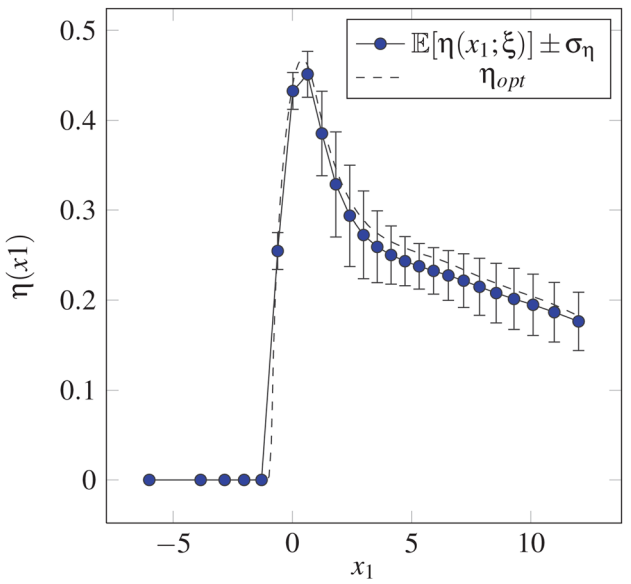

Fig. 12 Uncertainty in the spanwise-averaged film cooling effectiveness $\eta(x_1; \xi)$

variations is muted relative to the upstream locations. Further downstream, at $x_1 = 10$ the maximum of η shifts to higher blowing ratio (BR $\simeq 0.45$), and downstream of the peak in the $\mu(\xi)$ curve. However, the relatively wide region of flat η creates a low-sensitivity relationship between η and BR. This results in a fairly concentrated $\rho(\eta)$ and small value of standard deviation (see Fig. 11(*d*)).

In Fig. 12, the optimal film cooling effectiveness ($\eta_{\text{opt}}(x_1) \equiv \eta(x_1; \text{BR}_{\text{opt}} = 0.3)$ and the expectation ($\mathbb{E}[\eta(x_1; \xi)]$) of the spanwise-averaged film cooling effectiveness are shown. The streamwise axis is extended to include the jet hole and its upstream segment. The optimal effectiveness has higher values everywhere downstream of the jet. The vertical bars show the range of $\mathbb{E}[\eta(x_1; \xi)] \pm \sigma_\eta(x_1)$, where $\sigma_\eta(x_1)$ is the standard variation of $\eta(x_1; \xi)$. It is clear that the randomness of the blowing ratio

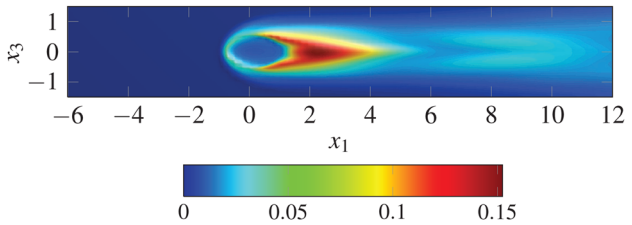

Fig. 13 Standard deviation of temperature, $\sigma_\theta(\mathbf{x})$ on the cooled surface of $x_2 = 0$

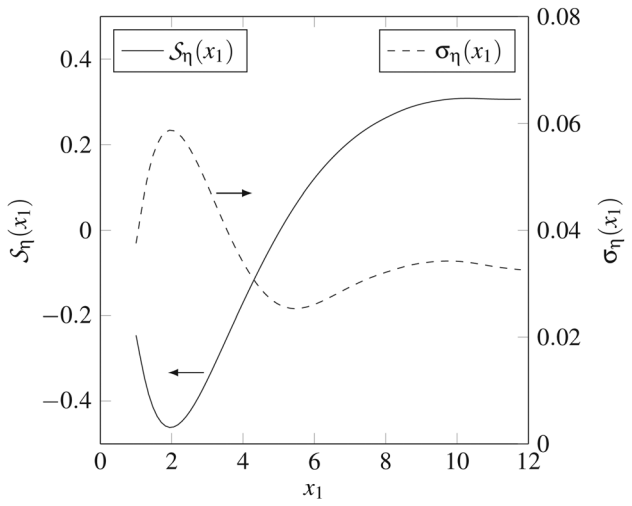

Fig. 14 Sensitivity and standard deviation of spanwise-averaged film cooling effectiveness $\eta(x_1; \xi)$

does not have any effect on the region upstream of the hole and therefore the standard deviation is zero in this segment. As it was demonstrated above, the random blowing ratio has the maximum impact near the jet trailing edge. The standard deviation decreases after $x_1 \geq 2.5$ and reaches a minimum near $x_1 = 6$ and then increases again till $x_1 \simeq 9.5$ and remains almost unchanged thereafter. This behavior is quantified in Figs. 13 and 14.

In Fig. 13, the contour plot of the standard deviation of temperature, $\sigma_\theta(\mathbf{x})$, is shown on the cooled surface of $x_1 = 0$. Note that the standard deviation of time-averaged temperature is also equivalent to the standard deviation of the local film cooling effectiveness, since $\bar{\theta}(x_1, 0, x_3; \xi) = 1 - \eta(x_1, x_3; \xi)$. The region immediately downstream of the jet hole has the largest amount of variability in film cooling effectiveness of $\sigma_\eta \simeq 0.15$, which is also equal to the relative variation of local film cooling effectiveness of $\sigma_\eta / \mathbb{E}[\eta] = 20\%$. Assuming typical engine operating conditions with $T_h = 1500°C$ and $T_c = 750°C$, $\sigma_\theta = 0.15$ translates to $\Delta\theta \simeq 110°C$ on the blade surface as a result of variation in blowing ratio.

Figure 14 shows the sensitivity and standard deviation of spanwise-averaged film cooling effectiveness. The highest magnitude of the sensitivity is reached at $x_1 = 2$, which also corresponds to maximum value of standard deviation, both re-affirming the existence of the high-sensitivity region downstream of the jet hole. It should be noted that $\mathcal{S}_\eta(x_1)$, is a measure of the *overall* sensitivity of $\eta(x_1; \xi)$ with respect to blowing ratio. As it can be seen in Fig. 10, $\eta(x_1; \xi)$ at $x_1 = 2$ has a large portion of negative slope coinciding with the high-probability region. This leads to the negative sign of sensitivity in this region. The magnitude of sensitivity decreases at $x_1 > 2$ and becomes zero at $x_1 \simeq 5$. At $x_1 \simeq 5$ (although not shown in Fig. 10), the maximum of $\eta(x_1; \xi)$ roughly occurs at the design point $\xi = 0.3$. This leads to a balanced distribution of positive- and negative-slope regions around $\xi = 0.3$ with a symmetric probability distribution around it. This means that the random $\eta(x_1; \xi)$ at $x_1 \simeq 5$ has equal samples of positive and negative slope of $d\eta/d\xi$ that have resulted in their cancellation and thus zero sensitivity is resulted. Note that the standard deviation reaches its minimum at roughly the same location of $x_1 \simeq 5$. At $x_1 \geq 5$, the positive-slope region outweighs the negative-slope region (see Fig. 10) resulting in positive sensitivities. The magnitude of the sensitivity also increases as the maximum of the $\eta(x_1; \xi)$ occurs at higher blowing ratios, resulting in a smaller negative-slope region. The value of standard deviation also increases due to the increasing offset between the maximum of $\eta(x_1; \xi)$ and $\mu(\xi)$.

5 Concluding Remarks

In this study, an efficient numerical algorithm for quantifying the effect of uncertainty of blowing ratio on film cooling performance has been presented. The geometry of the problem includes a plenum and a 35-deg inclined delivery tube. The blowing ratio is a random variable associated with a truncated Gaussian distribution with the mean of 0.3 and the standard deviation of 0.098. The multi-element general polynomial chaos is utilized to discretize the parametric space into non-overlapping elements and an orthogonal polynomial expansion within each element. A pseudo-spectral method has been used to find the expansion coefficients in a non-intrusive manner by sampling the governing equations at Gauss-quadrature points. The spectral element method has been used to perform direct numerical simulation at each quadrature point. The findings of this study can be summarized as:

(1) A probabilistic framework to quantify the effect of randomness in the blowing ratio on film cooling effectiveness is presented.
(2) Fast convergence of the the general polynomial chaos combined with capability of local refinement offered by ME-gPC method is as an effective strategy to evaluate the effect of uncertainty or randomness in the blowing ratio on the cooling performance.
(3) Using the approach in the current study, all the statistical information of the time-averaged quantities, such as probability density function, expectation and variance, sensitivity, etc can be calculated. This information can be integrated into a Bayesian approach for probabilistic design, and future studies at higher Reynolds number will explore these extensions into probabilistic design.
(4) The laterally-averaged cooling effectiveness has its maximum value closer to the trailing edge of the coolant hole. This maximum value occurs at a lower blowing ratio, and is associated with the largest variance.
(5) The expected values are lower than the design cooling effectiveness at the design BR of 0.3 and reflect the influence of the blowing ratio randomness.
(6) The standard deviation of the surface temperature indicates the randomness in blowing ratio causes the highest amount of temperature variation ($\sigma_\theta \simeq 0.15$) in the region extending from trailing edge of the exit hole to four diameters downstream. This amounts to 20% of relative variation of local film cooling effectiveness ($\sigma_\eta / \mathbb{E}[\eta]$) or equivalently the temperature variation of $\Delta\theta \simeq 110°C$ on the blade surface for typical engine conditions.
(7) The most and least sensitive regions to the variation in blowing ratio occur at two jet diameters and five jet diameters downstream of the hole, respectively.

Acknowledgment

This work was supported by grants from AFOSR, DEPSCoR-AFOSR, and DOE-CPERC programs. This support is gratefully acknowledged. The computations were performed on High Performance Computing systems at Louisiana State University. The second author (X.W.) was partially supported by NSF Grant DMS-1115632. The third author (S.A.) also appreciates the

support from the National Science Foundation (NSF) in the preparation of this work.

Nomenclature

B_e = random element
BR = blowing ratio
D = jet diameter
I_{Be} = indicator random variable at element, B_e
M = general polynomial chaos order
Ne = number of element in random space
p = pressure
Pr = Prandtl number
Re = Reynolds number
$\mathcal{S}$ = sensitivity with respect to random parameter
$\boldsymbol{u}$ = Cartesian velocity vector
$\boldsymbol{x}$ = Cartesian coordinate

Greek Symbols

η = spanwise-averaged adiabatic film cooling effectiveness
$\bar{\eta}$ = spatially-averaged adiabatic film cooling effectiveness
$\mu(\xi)$ = probability density function of random parameter
$\phi_i^e(\xi)$ = general polynomial chaos basis of order i at element e
σ = standard deviation
θ = normalized temperature
ξ = random parameter

Subscripts and Superscripts

$\widehat{(.)}$ = expansion coefficient
$(.)_M$ = orthogonal projection onto polynomial space of order
$\overline{(.)}$ = time average

References

[1] Han, J., Dutta, S., and Ekkad, S., 2001, *Gas Turbine Heat Transfer and Cooling Technology*, Taylor & Francis, London.
[2] Bogard, D. G., and Thole, K. A., 2006, "Gas Turbine Film Cooling," J. Propul. Power, **22**(2), pp. 249–270.
[3] Baldauf, S., Schulz, A., and Wittig, S., 2001, "High-Resolution Measurements of Local Effectiveness From Discrete Hole Film Cooling," ASME J. Turbomach., **123**(4), pp. 758–765.
[4] Bidan, G., Vezier, C., and Nikitopoulos, D. E., 2013, "Study of Unforced and Modulated Film-Cooling Jets Using Proper Orthogonal Decomposition—Part I: Unforced Jets," ASME J. Turbomach., **135**(2), p. 021037.
[5] Abhari, R. S., 1996, "Impact of Rotor–Stator Interaction on Turbine Blade Film Cooling," ASME J. Turbomach., **118**(1), pp. 123–133.
[6] Womack, K. M., Volino, R. J., and Schultz, M. P., 2008, "Combined Effects of Wakes and Jet Pulsing on Film Cooling," ASME J. Turbomach., **130**(4), p. 041010.
[7] Xiu, D., 2009, "Fast Numerical Methods for Stochastic Computations: A Review," Comm. Comp. Phys., **5**(2–4), pp. 242–272.
[8] Ghanem, R. G., and Spanos, P. D., 1991, *Stochastic Finite Elements: A Spectral Approach*, Springer-Verlag, New York.
[9] Xiu, D., and Karniadakis, G. E., 2002, "The Wiener–Askey Polynomial Chaos for Stochastic Differential Equations," SIAM J. Sci. Comput. (USA), **24**(2), pp. 619–644.
[10] Venturi, D., Wan, X., and Karniadakis, G. E., 2008, "Stochastic Low-Dimensional Modelling of a Random Laminar Wake Past a Circular Cylinder," J. Fluid Mech., **606**, pp. 339–367.
[11] Wan, X., and Karniadakis, G. E., 2005, "An Adaptive Multi-Element Generalized Polynomial Chaos Method for Stochastic Differential Equations," J. Comput. Phys., **209**(2), pp. 617–642.
[12] Wan, X., and Karniadakis, G. E., 2006, "Multi-Element Generalized Polynomial Chaos for Arbitrary Probability Measures," SIAM J. Sci. Comput. (USA), **28**(3), pp. 901–928.
[13] Acharya, S., Tyagi, M., and Hoda, A., 2006, "Flow and Heat Transfer Predictions for Film Cooling," Ann. N. Y Acad. Sci., **934**(1), pp. 110–125.
[14] Acharya, S., and Tyagi, M., 2003, "Large Eddy Simulation of Film Cooling Flow From an Inclined Cylindrical Jet," ASME Conference Proceedings, **2003**(36886), pp. 517–526.
[15] Peet, Y., and Lele, S. K., 2008, "Near Field of Film Cooling Jet Issued Into a Flat Plate Boundary Layer: LES Study, ASME Conference Proceedings, **2008**(43147), pp. 409–418.
[16] Iourokina, I. V., and Lele, S. K., 2005, "Towards Large Eddy Simulation of Film-Cooling Flows on a Model Turbine Blade Leading Edge," AIAA Paper No. 670.
[17] Guo, X., Schroder, W., and Meinke, M., 2006, "Large-Eddy Simulations of Film Cooling Flows," Comput. Fluids, **35**(6), pp. 587–606.
[18] Renze, P., Schroder, W., and Meinke, M., 2008, "Large-Eddy Simulation of Film Cooling Flows at Density Gradients," Int. J. Heat Fluid Flow, **29**(1), pp. 18–34.
[19] Babaee, H., Acharya, S., and Wan, X., 2013, "Optimization of Forcing Parameters of Film Cooling Effectiveness,"ASME Conference Proceedings, ASME.
[20] Muldoon, F., and Acharya, S., 2009, "DNS Study of Pulsed Film Cooling for Enhanced Cooling Effectiveness," Int. J. Heat Mass Transfer, **52**(13–14), pp. 3118–3127.
[21] Smirnov, A., Shi, S., and Celik, I., 2001, "Random Flow Generation Technique for Large Eddy Simulations and Particle-Dynamics Modeling," J. Fluids Eng., **123**(2), pp. 359–371.
[22] Xiu, D., 2007, "Efficient Collocational Approach for Parametric Uncertainty Analysis," Comm. Comp. Phys., **2**(2), pp. 293–309.
[23] Xiu, D., 2010, *Numerical Methods for Stochastic Computations: A Spectral Method Approach*, Princeton University, Princeton, NJ.
[24] Warburton, T., 1998, "Spectral/hp Element Methods on Polymorphic Domains," Ph.D. thesis, Brown University, Providence, RI.
[25] Karniadakis, G. E., and Sherwin, S. J., 2005, *Spectral/hp Element Methods for Computational Fluid Dynamics*, Oxford University, New York.